RESEARCH ARTICLE

ADVANCED
MATERIALS
INTERFACES
Open Access

www.advmatinterfaces.de

Bixbyite-Type Zirconium Tantalum Oxynitride Thin Films as Composition-Tunable High Refractive Index Semiconductors

Laura I. Wagner, Alessia Canever, Elise Sirotti, Chang-Ming Jiang, Frans Munnik, Verena Streibel, and Ian D. Sharp*

Multinary nitrides and oxynitrides offer a range of tunable structural and optoelectronic properties. However, much of this vast compositional space remains to be explored due to the challenges associated with their synthesis. Here, reactive sputter deposition is used to synthesize isostructural polycrystalline zirconium tantalum oxynitride thin films with varying cation ratios and systematically explore their structural and optical properties. All films possess the cubic bixbyite-type structure and *n*-type semiconducting character, as well as composition-tunable optical bandgaps in the visible range. Furthermore, these compounds exhibit remarkably high refractive indices that exceed a value 2.8 in the non-absorbing sub-bandgap region and reach 3.2 at 589 nm for Ta-rich compositions. Photoemission spectroscopy reveals non-uniform shifts in electron binding energies that indicate a complex interplay of structural and compositional effects on interatomic bonding. In addition to being high-index materials, the measured band edge positions of the films align favorably with the water oxidation and reduction potentials. Thus, this tunable materials family offers prospects for diverse optoelectronics application, including for production of photonic metamaterials and for solar water splitting.

1. Introduction

Nitrides present a fascinating space in materials design, offering desirable properties for a diverse range of applications, including ceramic hard coatings,[1] advanced materials for lighting,[2] catalysts for ammonia synthesis,[3] permanent magnets,[4] superconductors,[5] and optical materials for plasmonic and high-index applications.[6–9] While main-group nitride semiconductors (e.g., III-N compounds) are technologically well-established, semiconducting ternary transition metal nitrides (TMNs) remain much less explored, with limited experimental knowledge regarding their fundamental material properties.[10] In fact, close inspection of the extensive map of inorganic ternary nitrides published by Sun et al.[11] reveals that most studies on mixed cation TMNs focus on metallic nitride compounds with nitrogen-to-cation ratios of one or lower. However, semiconducting ternary TMNs hold great promise in terms of non-toxicity, tunable bandgaps, variable charge carrier densities, and efficient solar light absorption.[12–14] Yet, achieving semiconducting properties typically requires high nitrogen-to-cation ratios, which lead to high cation oxidation states, bound valence electrons, and low free charge carrier densities. Due to the lower electronegativity of nitrogen compared to oxygen and the stability of molecular dinitrogen, the synthesis of pure, oxygen-free nitrides, especially those with high nitrogen contents and exhibiting semiconducting properties, typically requires extreme conditions, such as high temperatures and pressures, as well as oxygen-free atmospheres.[10,11,15] Given these requirements, oxygen impurities are ubiquitous in TMNs. Nevertheless, it is not trivial to distinguish studies on pure nitrides from those of oxygen-containing nitrides or even oxynitrides since the amount of oxygen contained in a material denoted as a "nitride" is often not examined in detail. However, a careful consideration of oxygen impurity contents in nitride materials is imperative since different amounts of incorporated oxygen can lead to dramatic changes in their physical properties.[12,16,17] For example, oxygen is known to passivate recombination defects in some TMNs used for photoelectrochemical energy conversion[16] and to influence electronic properties, such as the band edge and Fermi level positions, bandgap, and charge carrier density.[12,18–22]

L. I. Wagner, A. Canever, E. Sirotti, V. Streibel, I. D. Sharp
Walter Schottky Institute
Technical University of Munich
85748 Garching, Germany
E-mail: sharp@wsi.tum.de

L. I. Wagner, A. Canever, E. Sirotti, V. Streibel, I. D. Sharp
Physics Department, TUM School of Natural Sciences
Technical University of Munich
85748 Garching, Germany

C.-M. Jiang
Department of Chemistry
National Taiwan University
Taipei City 106, Taiwan

F. Munnik
Institute of Ion Beam Physics and Materials Research
Helmholtz-Zentrum Dresden-Rossendorf (HZDR)
01328 Dresden, Germany

**ADVANCED
SCIENCE NEWS**

www.advancedsciencenews.com

**ADVANCED
MATERIALS
INTERFACES**
Open Access

www.advmatinterfaces.de

Indeed, in many instances, it is more precise to consider these materials as oxynitrides.

Reactive magnetron (co-)sputtering offers the possibility to fine-tune thin film compositions and related material properties by modulating the reactive gas mixtures and applied sputter powers.[23,24] Using this technique, our group has previously synthesized monometallic $Ta_2N_{3-y}O_y$ thin films with variable oxygen contents in the bixbyite-type structure.[12] Nearly oxygen-free, metastable Ta_2N_3 showed degenerate semiconducting properties while oxygen-containing $Ta_2N_{3-y}O_y$ exhibited non-degenerate semiconducting behavior due to charge compensation by oxygen anions incorporated at structural vacancy sites of the bixbyite lattice. Due to its moderate bandgap and favorable electronic structure, this oxygen-containing non-degenerate $Ta_2N_{3-y}O_y$ has been considered as a potential photoanode material for solar water splitting.[12,25] In addition, a related monometallic material is Zr_2N_2O.[26–28] Similar to Ta_2N_3, this compound crystallizes in the bixbyite-type structure, displays n-type character, has an optical bandgap that is tunable in the UV-visible range, and is photoactive for oxygen evolution under alkaline conditions.[27] Given the structural similarities of Zr_2N_2O and $Ta_2N_{3-y}O_y$, we now consider the possibility of generating a semiconducting phase with tunable electronic structure by combining Ta and Zr into a quaternary oxynitride compound.

As a starting point, we note that there have been a few attempts to grow zirconium tantalum nitride films using reactive magnetron co-sputtering. For example, Abadias et al.[24] and Aouadi et al.[29] successfully synthesized ternary metallic $Zr_{1-x}Ta_xN$ films with the cubic rocksalt-type structure, with the resulting materials exhibiting a high hardness.[24] The metallic film properties likely resulted from their comparatively large cation-to-anion ratios compared to nitrogen-rich compounds that would be expected to have semiconducting character. In contrast, Lüdtke et al.[30] performed bulk ammonolysis of amorphous Ta- and Zr-based precursors to synthesize crystalline bixbyite-type powders with optical bandgaps between 1.30 and 1.72 eV, showing that both structural and optical properties vary with the O and Zr contents.

Recently, we synthesized bixbyite-type $ZrTaN_3$ thin films via reactive magnetron co-sputtering and observed a strong optical absorption onset at 1.8 eV, along with significant photoactivity.[31] In that work, we demonstrated that this material is an n-type semiconductor suitable for photoelectrochemical applications, with optoelectronic properties governed by cation site symmetry and disorder. In particular, the bixbyite structure features two inequivalent cation lattice sites with differing symmetry, given by Wyckoff sites 8b and 24d, with the bandgap predicted to increase with decreasing amount of Ta occupying the 24d Wyckoff site. While that work focused on intrinsic disorder (i.e., the exchange of cation sites with fixed elemental ratio [32]) in stoichiometric $ZrTaN_3$ thin films with low oxygen content, we now investigate the role of extrinsic disorder, in the form of non-stoichiometric cation and oxygen anion contents, on the optical and electronic properties of this emerging class of semiconductors. For example, assuming statistically evenly distributed cations on the inequivalent Wyckoff sites,[31] we now seek to tune the Wyckoff site occupancy via the cation composition, exploiting extrinsic disorder to modulate the bandgap.
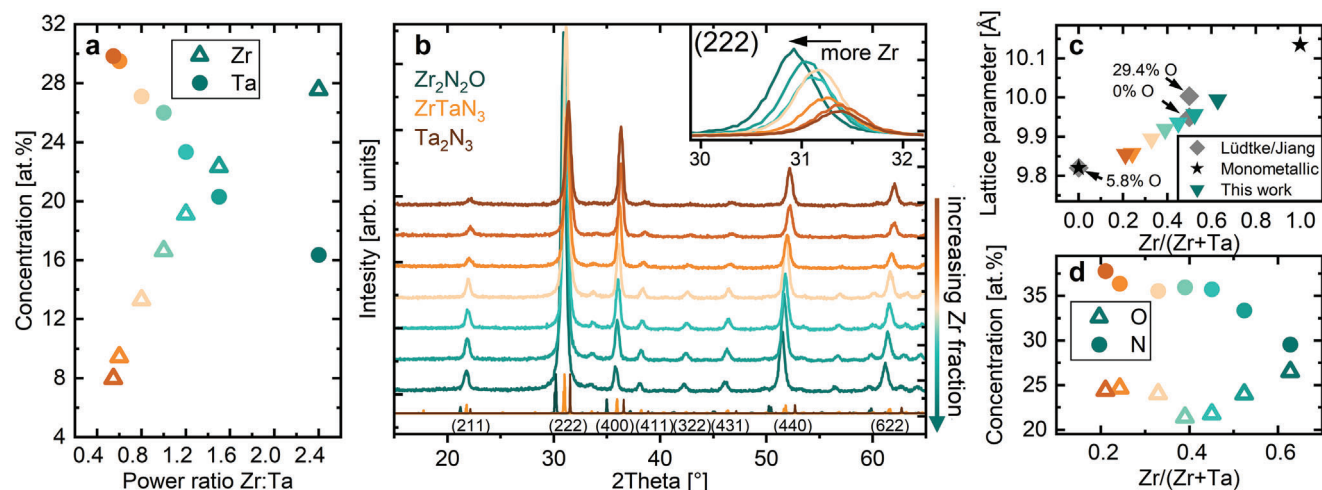
Herein, we demonstrate the successful synthesis of a library of semiconducting zirconium tantalum oxynitride thin films by reactive sputter deposition. Through a careful choice of deposition parameters, we obtain polycrystalline thin films in the bixbyite-type structure with a varying cation ratio (Zr/(Zr+Ta)) but similar thickness and morphology. In this well-defined materials library, we experimentally explore the effect of composition on the structural and optical properties, as well as the electronic structure and photoactivity. Detailed compositional and structural characterization reveals the isostructural nature of all films, with the cubic bixbyite lattice parameter varying linearly with the cation composition ratio. Non-uniform shifts in the XPS core level binding energies of the anions and cations indicate charge redistribution as the composition changes. Combined UV-Vis absorption spectroscopy and variable angle spectroscopic ellipsometry reveal an increasing optical absorption onset and decreasing refractive index with increasing Zr content. Importantly, the transparent sub-bandgap region is characterized by a low extinction coefficient (<0.1) and a high index of refraction (>2.8). The index increases with decreasing oxygen and zirconium content in the films, exhibiting a remarkably large value of up to 3.2 at 589 nm. Chopped-illumination contact potential difference (CPD) measurements indicate that the films are photoactive semiconductors with n-type character. Thus, these compounds are characterized by broadly composition-tunable optical and electronic properties, with large indices and non-degenerate semiconducting character that are well suited for use in optical coatings and for fabrication of optical metamaterials.

2. Experimental Results

2.1. Controlling Composition and Structure of $Zr_xTa_{2-x}N_{3-y}O_y$ Thin Films

Bixbyite-type $Zr_xTa_{2-x}N_{3-y}O_y$ thin films with different Zr to Ta ratios were synthesized by reactive magnetron co-sputtering using metallic Zr and Ta targets. All films were deposited on fused silica and n$^+$-Si substrates at substrate temperatures set to 500 or 600 °C and a process pressure of 6.5 mTorr. The reactive gas mixture consisted of 33.1% Ar, 66.1% N_2, and 0.8% O_2. We carefully introduced such small amounts of oxygen during the sputter deposition to make use of the oxygen-inductive effect, which allows us to access higher cation oxidation states and achieve semiconducting film properties, as previously established for the $Ta_2N_{3-y}O_y$ system.[12] To achieve varying Zr to Ta ratios at similar film thicknesses, applied sputter powers and deposition times were adjusted, as summarized in Table S1 (Supporting Information). The desired film thickness of ≈100 nm was confirmed by fitting of variable angle spectroscopic ellipsometry (VASE) data. Additional details regarding the synthesis conditions can be found in the experimental details section.

To evaluate the surface chemical composition and confirm the intended variations in Zr and Ta contents, we performed X-ray photoelectron spectroscopy (XPS). **Figure 1a** displays the concentrations of Ta and Zr obtained with varying Zr:Ta sputter power ratios during deposition. With increasing Zr:Ta power ratio, the concentration of Zr increases from 8 to 28 at.% while the concentration of Ta decreases from 30 to 16 at.%. Based on these results, the samples discussed below are designated by their Zr

**ADVANCED
SCIENCE NEWS**

www.advancedsciencenews.com

**ADVANCED
MATERIALS
INTERFACES**
Open Access

www.advmatinterfaces.de

Figure 1. Structural and compositional analysis of $Zr_xTa_{2-x}N_{3-y}O_y$ thin films. a) Zr and Ta concentrations depend on the Zr:Ta power ratio applied during synthesis via reactive co-sputtering. b) GI-XRD patterns of as-deposited thin films with varying Zr:Ta ratios. All diffraction patterns match the bixbyite-type references[12,30,33] and display a consistent shift to lower scattering angles with increasing Zr content. The inset demonstrates the change in both the (222) reflection angle and strength with changing Zr fraction. c) Change of the cubic bixbyite lattice parameter with Zr content (triangles). For comparison, monometallic references (stars),[33,34] and experimental powder/polycrystalline diffraction results from Lüdtke et al.[30] and Jiang et al.[12] are added as grey squares, together with their respective oxygen contents. d) N and O concentrations determined via XPS as a function of the Zr cation fraction (Zr/(Zr+Ta)).

cation fraction, defined by Zr/(Zr+Ta), where Zr and Ta represent the respective metal atomic percent obtained from XPS measurements. The data set presented in this work contains seven samples, with Zr cation fractions ranging from 0.21 to 0.63.
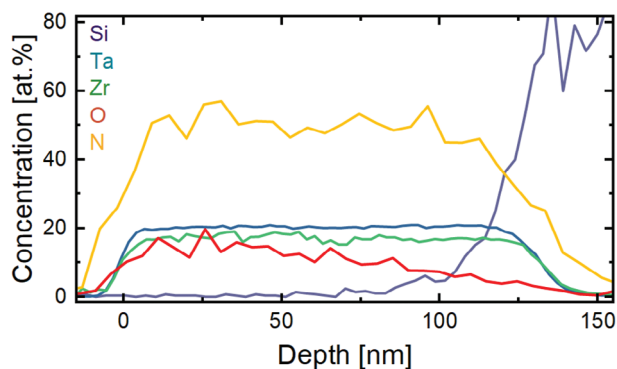
The grazing incidence X-ray diffraction (GI-XRD) patterns of all samples are in good agreement with bixbyite-type phases, exhibiting features similar to the related compounds Ta_2N_3, $ZrTaN_3$, or Zr_2N_2O, but with composition-dependent diffraction angles and strengths (Figure 1b). Indeed, we observe no unidentified reflections, confirming the successful synthesis of a compositionally tunable library of polycrystalline cubic bixbyite-type $Zr_xTa_{2-x}N_{3-y}O_y$ thin films. The XRD full width at half maximum (FWHM) lies between 0.51° and 0.56° for all samples, with a minimum observed for the film with a Zr:Ta ratio close to 1:1 (i.e., Zr/(Zr+Ta) = 0.5). A rough estimate via the Scherrer equation[35] suggests similar grain sizes for all films, ranging from 14 to 17 nm and with a mild trend towards larger grain sizes with higher Zr contents (Figure S1, Supporting Information). Complementary atomic force microscopy (AFM) images show planar, polycrystalline morphologies for all films with round, evenly distributed grains. The roughness ranges from 0.9 to 2.3 nm, with a maximum close to a Zr cation fraction of 0.5. Consistent with XRD analysis, AFM-based particle size analysis reveals grain sizes between 15 and 25 nm, where the grain size again increases with increasing Zr content (Figures S1 and S2, Supporting Information).

After confirming a similar morphology for all samples, we now consider the thin film diffractograms in more detail. With increasing Zr content, the height of the (400) reflection decreases while the (222) reflection increases, as highlighted by the inset of Figure 1b. Comparing the relative peak heights within each pattern with the reference patterns of Ta_2N_3,[12] $ZrTaN_3$,[30] and Zr_2N_2O,[33] we observe a shift towards increasingly oriented films with increasing Zr incorporation. While the height ratio of the

(222) and (400) reflections remains similar at a value of 1.4 for Ta-rich samples, this ratio increases up to 16.3 for Zr-rich samples. However, all diffraction planes can be resolved clearly throughout our entire library, indicating poly-crystalline films with different preferred orientations.

In terms of reflection angles, we observe a clear shift of all reflections to lower angles with increasing Zr content, as illustrated for the (222) reflection in the inset of Figure 1b. In accordance with Vegard's law, the lattice constant calculated from the peak positions increases linearly, from 9.85 Å to 9.99 Å, with increasing Zr content (Figure 1c).[36] These calculated lattice constants align with a linear interpolation between the lattice constants of the limiting monometallic bixbyite-type compounds of 9.82 Å for Ta_2N_3[34] and 10.14 Å for Zr_2N_2O (black stars).[33] The lattice constant for Ta_2N_3 thin films, previously obtained within our group by Jiang et al.[12] using similar deposition conditions (grey square), matches the literature-reported value.[34] The observed increase in lattice constant with Zr content can be rationalized by the different ionic radii of Zr^{4+} (72 pm) and Ta^{5+} (64 pm).[37] Increasing the Zr concentration requires more space within the lattice to isostructurally accommodate the larger Zr ions. Such a lattice constant increase with Zr content has also been reported in previous studies of orthorhombic Zr-Ta-O-N[37] and rocksalt-type $Zr_{1-x}Ta_xN$.[24] In addition, our values align well with the lattice constants reported by Lüdtke et al.[30] for oxygen-free and 30 at.% oxygen-containing powder samples, marked by grey squares in Figure 1c.

Having analyzed the impact of different cation ratios on structure, we now shift our attention to the anion concentrations within this library of $Zr_xTa_{2-x}N_{3-y}O_y$ thin films. As a starting point, we determined the surface concentrations of oxygen and nitrogen with XPS (Figure 1d). For all films, we observe a higher concentration of nitrogen than oxygen, with nitrogen amounting to 30–38 at.%, and oxygen to 21–27 at.%. While the Ta-rich

**ADVANCED
SCIENCE NEWS**

www.advancedsciencenews.com

**ADVANCED
MATERIALS
INTERFACES**
Open Access

www.advmatinterfaces.de

Figure 2. Composition profiles, presented as elemental concentrations, as a function of depth below the film surface, obtained by elastic recoil detection analysis of a $Zr_xTa_{2-x}N_{3-y}O_y$ layer with a Zr cation fraction of 0.5 and grown on a Si substrate.

samples (Zr/(Zr+Ta) ⩽ 0.5) display a high N/O ratio of approximately 1.5, Zr-rich samples show increasing oxygen incorporation and decreasing N/O ratios. The generally high oxygen concentration of more than 20 at.% may seem surprising considering the low fraction of O_2 in the reactive gas mixture (⩽1%). However, XPS is a highly surface-sensitive technique and nitrides tend to form surface oxide layers when exposed to ambient conditions.[23,38,39] In addition, oxygen is considerably more reactive than nitrogen[40] and zirconium has a very high oxygen affinity.[41] For these reasons, oxygen incorporation cannot be avoided during the co-sputtering process of our $Zr_xTa_{2-x}N_{3-y}O_y$ thin films, where small quantities of oxygen are required to achieve the high cation oxidation states necessary for semiconducting film properties.[12,27,42] While much of the surplus oxygen can be driven out of similar nitride thin films by post-deposition annealing treatments in ammonia,[12,17] such annealing treatments are not part of the current study, in which we intentionally focus on oxynitride compounds.

To quantify the anion ratio in the bulk, we next used energy-dispersive X-ray spectroscopy (EDX), which confirms the observed trends of chemical composition, with estimated total nitrogen contents between 55 and 65 at.% and oxygen contents between 20 and 32 at.% (Figure S3, Supporting Information). Compared to XPS, the EDX results generally show a higher N/O ratio of 2–3 (Figure S4, Supporting Information). In terms of absolute concentrations, however, EDX tends to overestimate light elements compared to heavier elements; in the present case, the anions are overestimated compared to the cations.[43] Hence, the true bulk oxygen composition is expected to be even lower. To calibrate the measured concentration obtained from EDX, we performed elastic recoil detection analysis (ERDA) on a sample synthesized with a near 1:1 ratio of Zr:Ta. For this sample, we obtain an oxygen concentration from ERDA of only 10–15 at.% in the bulk compared to 21 at.% by EDX. Comparing to our XPS measurements discussed above, we thus confirm a higher oxygen fraction at the surface than in the bulk. In addition, the ERDA composition profile reveals an increasing oxygen gradient from the substrate towards the surface of the film (**Figure 2**). In particular, the oxygen concentration increases from approximately 7 at.% at the bottom to 16 at.% at the surface of the layer. We note here that, while we do observe an oxygen gradient within
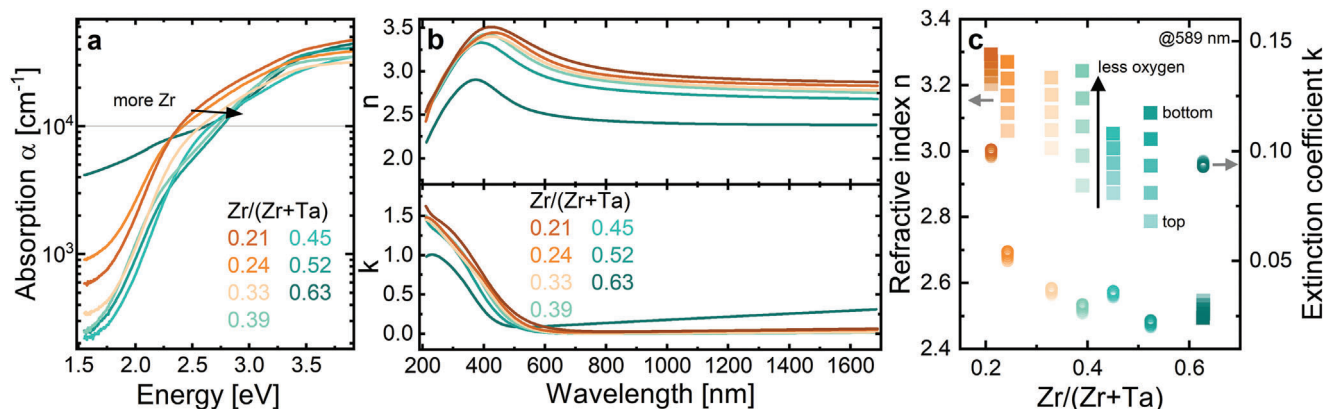
the material, the cation concentrations are constant throughout the film thickness and agree well with the values obtained from XPS quantification. The Zr fraction appears slightly underestimated in the ERDA traces due to shielding of atomic nuclei by the electron cloud of heavy atoms. This results in a comparatively large uncertainty in the cation elemental ratio obtained by ERDA. However, XPS of this sample confirmed the 1:1 Ta:Zr ratio.

To summarize, we have created a library of compositionally tunable, isostructural bixbyite-type $Zr_xTa_{2-x}N_{3-y}O_y$ thin films with similar grain sizes and Zr content-dependent oxygen concentrations. The lattice constants of these films increase linearly with Zr cation fraction, consistent with the observation from Lüdtke et al.[30] Moreover, for a Zr:Ta ratio of approximately 1:1, the calculated lattice constant agrees well with that prior report on Zr-Ta-O-N powder samples.[30] In the following, we set out to characterize the impact of these varying cation and anion contents on the optical and electronic properties of the films.

2.2. Optical Properties of High Index Coatings

To assess the bandgaps of the $Zr_xTa_{2-x}N_{3-y}O_y$ thin films, we performed optical absorption measurements with a diffuse reflectance sphere of a UV-vis spectrophotometer (**Figure 3a**). These measurements reveal a clear absorption edge that shifts towards higher energies with increasing Zr concentration, indicating semiconducting character with composition-tunable bandgaps. Considering the limitations of Tauc analysis,[44] we used the iso-absorption E04 method[45] to assess the optical bandgap, which is approximated to occur at an absorption threshold of 10^4 cm^{-1}. Using this approximation, we observe an increase in bandgap from 2.4 eV for the 0.21 sample to 2.8 eV for the 0.52 sample, demonstrating a widening bandgap with increasing Zr content. However, we note that these values are likely overestimates, with analysis of the linearly plotted absorption edge and Tauc plots (Figure S5a,b, Supporting Information) indicating absorption onsets in the range from 1.9 to 2.4 eV. Nevertheless, all results indicate a similar trend with composition. In addition to this bandgap opening, the sub-bandgap absorption tends to decrease with increasing Zr content, suggesting a decrease of mid-gap defect states or free carrier concentrations. However, the 0.63 sample, containing the highest Zr content, displays a deviation from these trends, with a bandgap of only 2.6 eV and a higher sub-bandgap absorption. These deviations may be related to an increased concentration of metallic defects. In particular, we have previously found that, sputtering of Zr_2N_2O requires a slightly higher oxygen dose compared to $Ta_{2-x}N_{3-y}O_y$ to achieve crystalline, semiconducting thin films.[12,27] Hence, in this high Zr content sample, the chosen constant gas mixture within our sample library likely provided insufficient oxygen, resulting in an oxygen deficiency and the formation of metallic ZrN or TaN secondary phases.

From an electronic structure perspective, two factors most likely lead to the increasing bandgap with increasing Zr content. First, for Zr-rich films, the oxygen content increases with Zr content, which is expected to drive the valence band maximum to more negative energies. However, only small changes of oxygen content are observed for the Ta-rich compounds, suggesting that the cation ratio itself influences the bandgap. Thus, we

ADVANCED
SCIENCE NEWS

www.advancedsciencenews.com

ADVANCED
MATERIALS
**INTERFACES**

www.advmatinterfaces.de

Figure 3. Optical properties of $Zr_xTa_{2-x}N_{3-y}O_y$ thin films. a) Absorption spectra obtained from UV-vis measurements. b) Optical constants, n and k, as a function of Zr cation fraction obtained by modeling of variable angle spectroscopic ellipsometry (VASE) data using a graded five-layer model to account for the oxygen concentration gradient within the films. The presented optical constants are those from the middle layer (slice 3). c) Refractive index, n (squares), and extinction coefficient, k (circles), of each layer of the VASE fit using a graded model, evaluated at 589 nm as a function of the Zr cation fraction. The symbols increase in color intensity according to depth within the layer, from the top to bottom surface.

consider a second contribution to the changing electronic structure. That is, assuming a statistically even distribution of Ta and Zr on the two inequivalent cation sites, increasing Zr content will lead to decreased Ta occupation of the 24d Wyckoff site, which has been predicted to lead to an increase of the conduction band minimum position and opening of the bandgap in bixbyite-type $ZrTaN_3$.[31] In this regard, the present results are consistent with prior density functional theory (DFT) calculations of the influence of cation site occupancy on the electronic structure of the pure nitride analogue $ZrTaN_3$. Importantly, since the oxygen content in $Zr_xTa_{2-x}N_{3-y}O_y$ can be independently tuned by post-synthetic ammonolysis, these results highlight the versatility of this material for both bandgap and band edge energetic tuning. In particular, increasing Zr contents are expected to lead to an upwards energetic shift of the conduction band minimum, while increasing oxygen concentrations would result in a downwards shift of the valence band maximum.

To determine the extinction coefficients, k, and refractive indices, n, of our $Zr_xTa_{2-x}N_{3-y}O_y$ thin films, we measured variable angle spectroscopic ellipsometry (VASE). Fitting was performed using a generalized oscillator model consisting of a Cody-Lorentz-oscillator to account for the band-edge optical transition, a Drude(RT)-oscillator to describe the sub-bandgap absorption, and a PSemi-M0-oscillator for the behavior far above the bandgap.[46,47] In addition, we accounted for depth-dependent variations in the thin film properties using a graded layer approach. Such a grading was necessary to obtain a suitable fit and is consistent with the oxygen composition gradient observed by ERDA depth profiling of $ZrTaN_{3-y}O_y$ (Figure 2), as well as a previous study on Zr_2N_2O.[27] This oxygen gradient likely stems from variations of the gas atmosphere during growth caused by initial gettering of oxygen in the deposition chamber by the metals,[27] resulting in a corresponding depth-dependence of the optical constants. While beyond the scope of the current study, we hypothesize that this non-intentional composition gradient can be attenuated or even prevented by active tuning of gas compositions during film growth or by post-deposition annealing treatments.

To assess the impact of the cation ratio on the optical constants, we compare n and k of the middle layer of the composition gradient model for all films within our library (Figure 3b). In general, the optical constants of all films display a similar behavior, with low extinction in the sub-bandgap region and the onset of strong absorption at wavelengths shorter than the bandgap transition. Due to Kramers–Kronig consistency, the refractive index, n, correspondingly increases in the near-bandgap spectral range. At wavelengths longer than the bandgap transition, the extinction coefficient remains low for all but the most Zr-rich film (0.63, as discussed above), which likely contains a secondary metallic phase. Within the transparent region, all $Zr_xTa_{2-x}N_{3-y}O_y$ thin films display an extraordinarily high refractive index of around 2.8, with a simultaneously low k (<0.1).

At 589 nm, a common reference wavelength for reporting n,[48] the refractive index increases from 2.8 to 3.2 with decreasing Zr fraction (Figure 3c). The sample with 0.63 Zr cation fraction again represents an outlier, with a considerably lower index of 2.5, which is likely caused by free carrier absorption of the secondary metallic defect phase. Analysis of the graded model of each thin film reveals an increase of n with increasing depth below the surface when the Zr cation fraction is below 0.5. Since the cation ratio is constant but the oxygen content decreases with depth, application of the graded model across different films provides a means of assessing the impact of both cation and anion effects on the optical constants. Combining these observations, we conclude that the index increases with decreasing oxygen content and with decreasing Zr content within $Zr_xTa_{2-x}N_{3-y}O_y$ thin films. Interestingly, the extinction coefficient, k, shows a weaker dependence on the depth and, thus, oxygen content, exhibiting a minimum at an intermediate Zr cation fraction. Overall, these results reveal a large n and small k in the sub-bandgap range, suggesting that $Zr_xTa_{2-x}N_{3-y}O_y$ thin films are highly promising as tunable, high-index coatings for optical applications. Considering other high-index materials, such as GaAs, ZnSe, GaN or Si_3N4, with refractive indices in the visible/near-infrared region of 3.4, 2.5, 2.2, and 2.0, respectively,[6] the tantalum zirconium oxynitride system compares favorably while offering versatile
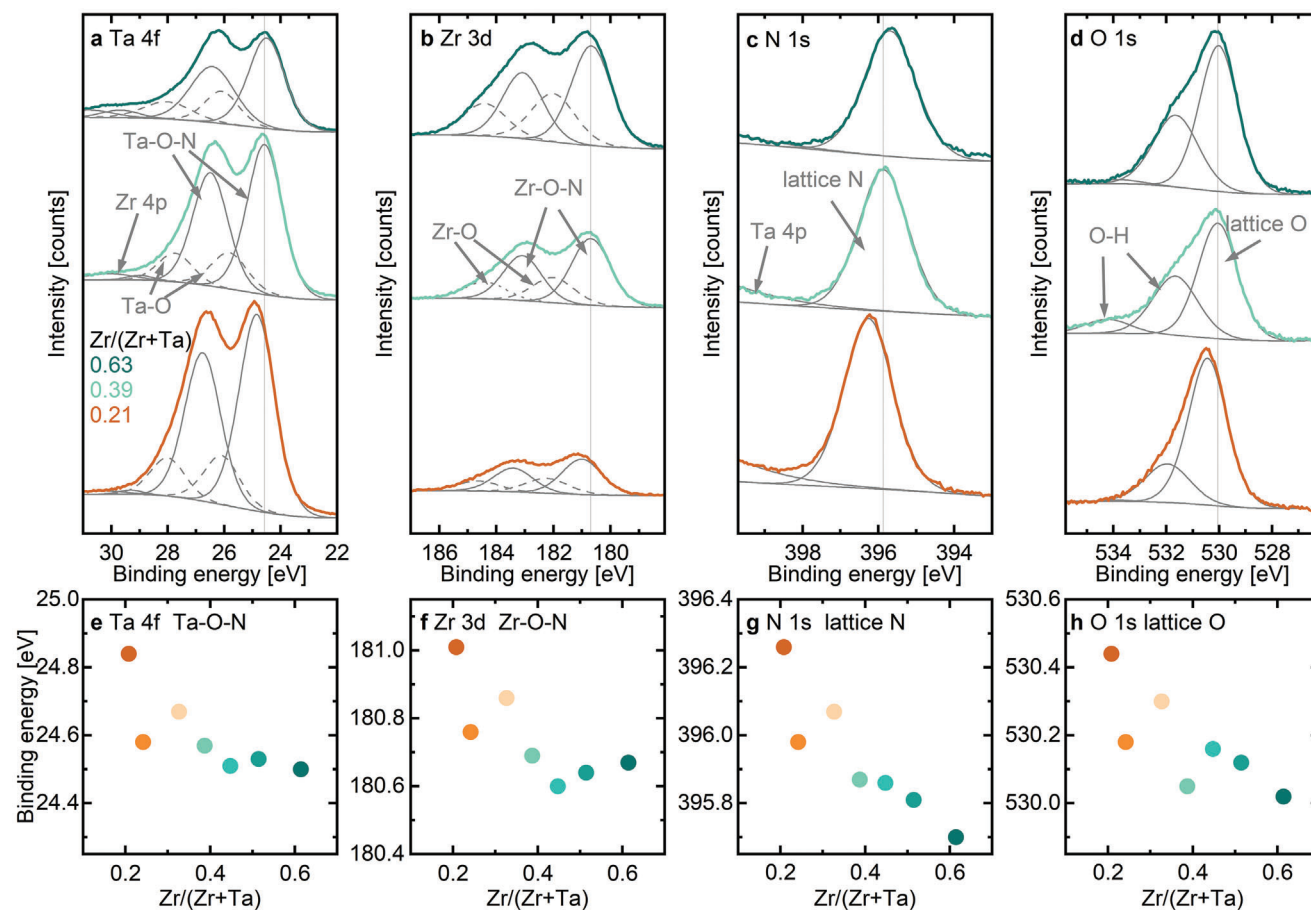
Figure 4. X-ray photoelectron spectra from a) Ta 4f, b) Zr 3d, c) N 1s, and d) O 1s core level regions for the $Zr_xTa_{2-x}N_{3-y}O_y$ samples with $Zr/(Zr+Ta)$ cation fractions of 0.21, 0.39, and 0.63. For all figures, the same color code is used, with the thin gray components representing the fitted peak deconvolution. The position of the most prominent peaks from the 0.39 Zr fraction sample are marked by vertical gray reference lines. e) Ta $4f_{7/2}$ Ta-O-N component, f) Zr $3d_{5/2}$ Zr-O-N component, g) N 1s lattice N component, and h) O 1s lattice O component binding energies as a function of the Zr cation fraction.

composition tunability, comprising non-toxic elements, and providing routes to scalable and low-cost synthesis of functional films.

2.3. Electronic Structure Changes with Composition

Having established the structural and optical tunability of our $Zr_xTa_{2-x}N_{3-y}O_y$ thin films, we now examine how compositional variations impact their electronic structures. **Figures** 4a–d display the XPS core level regions (Ta 4f, Zr 3d, N 1s, and O 1s) at three different cation ratios (0.21, 0.39, 0.63). The fitting of individual photoemission components within these regions is given by the thin gray lines. The Ta 4f core level spectra (Figure 4a) exhibit two peaks centered near binding energies (BEs) of 24.9 and 26.6 eV. The spectra can be deconvoluted into two spin-orbit split doublet contributions from Ta–O–N and Ta–O bonding, with Ta-O bonding found at higher BEs. Similarly, the Zr 3d region in Figure 4b exhibits two peaks centered near 180.7 and 183.0 eV, which can again be deconvoluted into two spin-orbit split doublet contributions from Zr–O–N and Zr–O species. For both Ta 4f and Zr 3d,

the oxynitride (–O–N) peaks outweigh the purely oxide-related (–O) peaks, indicating an even distribution of oxygen in the compound, with both oxygen and nitrogen bonding to Ta and Zr. In addition, lattice nitrogen and oxygen in the N 1s and O 1s core levels can each be fitted with one peak, but overlap at the high BE sides with the Ta 4p core level and O–H contributions from adsorbed water and hydroxyl groups, respectively (Figures 4c,d). With our experimental setup, it is not possible to discern between (–O) and (–O–N) contributions to the O 1s spectra, as also observed for the monometallic Zr_2ON_2 system.[27]

Comparing the core level spectra recorded for different cation ratios, we observe peak shifts to lower BEs with increasing Zr content. While this shift occurs in all core level regions, it is most clear in the N 1s region, with a $\Delta BE = -0.6$ eV. In contrast, the positions of the peaks attributed to –O–N bonding in both Zr 3d and Ta 4f regions shift by $\Delta BE = -0.3$ eV, while the O 1s component of lattice oxygen shifts by $\Delta BE = -0.4$ eV with increasing Zr cation fraction (Figures 4e,h). We note that this data set was calibrated to the C 1s peak, whose BE was fixed at 284.8 eV. Corresponding data, analyzed without applying such a correction but instead using only the standard Au calibration of the analyzer, are

**ADVANCED
SCIENCE NEWS**

www.advancedsciencenews.com

**ADVANCED
MATERIALS
INTERFACES**
Open Access

www.advmatinterfaces.de

provided in Figure S6 (Supporting Information), together with the valence band (VB) spectra obtained using both approaches. Both data sets display a similar trend, confirming that the observed shifts stem from the shifting of core levels with respect to the Fermi level rather than from charging or changing conductivity of the bixbyite-type $Zr_xTa_{2-x}N_{3-y}O_y$ thin films. In contrast to the observed shifts of the core level positions, fitting the VB maximum with respect to the Fermi level yields no clear shift with increasing Zr fraction (Figure S6c,f, Supporting Information). For all cation ratios, we observe a VB position that is roughly 0.9 eV below the Fermi level, hinting at non-degenerate semiconducting film properties. This approximately constant VB position can be explained by Fermi level pinning due to surface oxidation, which is commonly observed in tantalum nitride thin films after air exposure.[39,49] Despite such Fermi level pinning, we find that the energy difference between the VB maximum and the core levels decreases with increasing Zr content. Thus, the observed core level shifts are not a consequence of a changing Fermi level, but instead indicate composition-dependent changes in local charge density associated with the underlying electronic structure and bonding in the material.

Small composition- and lattice constant-dependent binding energy shifts have been previously reported for other mixed metal cation thin films, such as $Zn_xMg_{1-x}S:Mn$[50] and $Cr_{1-x}Ti_xN_y$.[51] Both systems exhibit an increase in BE with decreasing lattice parameter. For the case of $Zn_xMg_{1-x}S:Mn$, this behavior was attributed to composition-dependent atomic packing and the flexibility of its covalent bonds,[50] while for $Cr_{1-x}Ti_xN_y$, such an effect was assigned to an increase in charge transfer from the metal to the nitrogen atom, causing a positive shift of the BEs of metal states.[51] Analogously, we observe a general trend of decreasing binding energy with increasing lattice parameter, i.e., with increasing Zr content. This observation is consistent with expectation, where the increased lattice constant leads to decreased orbital overlap and, thus, decreased BEs.[52,53] However, the shift is stronger for the lattice oxygen and nitrogen than for the cations, suggesting that an additional factor contributes to the observed core level positions. In particular, differing compositions can lead to changes of the bond polarity, resulting in additional shifts of cation and anion core level positions that act in opposite directions. Here, the addition of Zr reduces the average electronegativity of the cations, while increased oxygen content increases the average electronegativity of the anions. Such changes are expected to enhance charge transfer from cations to anions, resulting in an increase (decrease) of the core level BEs of Ta and Zr (O and N). Thus, both lattice parameter and bond polarity changes lead to BE shifts in the same direction for anion core levels, while these two contributions counteract one another for the case of cation core levels. As a result, stronger composition-dependent shifts are observed for anion compared to cation BEs. Finally, we note that different degrees of cation and anion disorder have been shown to impact the bandgaps of mixed cation oxynitride systems and may also impact the core level binding energies in non-trivial ways.[32,54]

To determine the work functions and investigate the surface band bending of our $Zr_xTa_{2-x}N_{3-y}O_y$ thin films, we performed contact potential difference (CPD) measurements (**Figure 5** and Figure S7, Supporting Information) in the dark and under illumination. All dark values lie close to 150 mV ± 50 mV versus
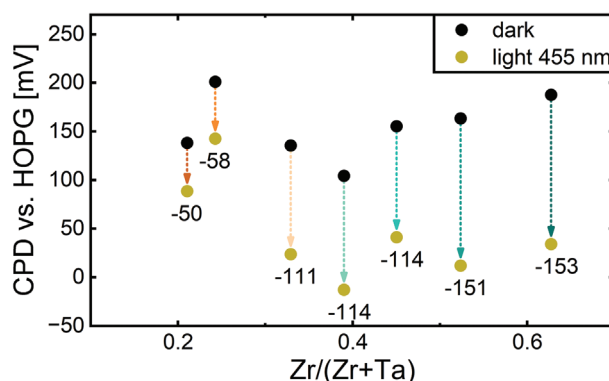
Figure 5. Results from surface photovoltage measurements. Comparison of the contact potential difference (CPD) in dark (black) and under illumination (yellow) as a function of the Zr cation fraction within $Zr_xTa_{2-x}N_{3-y}O_y$ thin films. The numbers below the data points give the magnitude of SPV in mV.

the highly oriented pyrolytic graphite (HOPG) reference used for measurement calibration, yielding a work function of all $Zr_xTa_{2-x}N_{3-y}O_y$ thin films close to that of HOPG in air ($\approx$ 4.5 eV).[55] Considering the hydrogen (HER) and oxygen evolution reaction (OER) potentials, located at 4.44 and 5.67 eV,[56] we find the Fermi levels of our thin films to be between these potentials, with the VB position located very close to the OER potential and the CB above the HER potential, suggesting a possible application of $Zr_xTa_{2-x}N_{3-y}O_y$ as thin film photoelectrodes or particle-based photocatalysts for solar water splitting.[57]

While the dark work functions exhibit no clear trend with cation ratio, we observe a monotonic increase in surface photovoltage with increasing Zr content. When illuminated with above bandgap radiation using a 455 nm LED, all $Zr_xTa_{2-x}N_{3-y}O_y$ films show a negative surface photovoltage (SPV), typical for *n*-type semiconductors with upward surface band bending.[58] In particular, Ta-rich films exhibit a small SPV of 50 mV, while the film with 0.63 Zr cation fraction displays a large SPV of 153 mV. The observed increase of SPV with increasing Zr content can be related to enhanced quasi-Fermi level splitting due to increased surface band bending and/or reduced recombination at defects.[23,59] Overall, these measurements indicate that all films are photoactive, which, together with the near mid-gap Fermi energy obtained from VB spectroscopy, indicates that these materials are non-degenerate semiconductors.

3. Conclusion

Using reactive sputtering, we successfully synthesized a library of polycrystalline, semiconducting $Zr_xTa_{2-x}N_{3-y}O_y$ thin films with broadly tunable Zr/(Zr+Ta) cation ratios, all of which possess the cubic bixbyite-type structure. In this library, we observe tunable variations in fundamental material properties based on their cation compositions. In particular, the thin films display a linear increase in lattice parameters, optical bandgaps, and surface photovoltages with increasing Zr/(Zr+Ta) cation ratios. All films exhibit remarkably large refractive indices, with values near 2.8 across the transparent region and reaching 3.2 at 589 nm. The index tends to increase with decreasing Zr fraction

and O content within the films, enabling compositional tuning of this key optical property. While we did not explicitly investigate the effect of varying oxygen concentrations on material properties, we identify opportunities for further tuning functional characteristics by controlling anion composition during synthesis or via post-synthetic ammonia annealing treatments. Overall, our finding that isostructural $Zr_xTa_{2-x}N_{3-y}O_y$ thin films can be synthesized over a wide range of compositions, together with their tunable optoelectronic properties and favorable energetic band edge positions, provide promise for a variety of optoelectronic applications, ranging from refractive coatings and metamaterials for advanced photonics to their use in photoelectrochemical or photocatalytic energy conversion systems.

4. Experimental Section

All thin films were deposited using reactive magnetron co-sputtering on single-side polished n^+-doped Si (Siegert Wafer, Prime) with a resistivity below 0.005 Ω cm and on double-side polished fused silica (Siegert Wafer, Corning 7980). The use of both substrates enabled measurements requiring either insulating, transparent, or conducting substrates. In particular, XRD, XPS, and SPV were performed on n^+-Si, while AFM, UV–vis, and VASE were measured on fused silica. On both substrates, the films show similar crystallinity and structural properties for the same cation composition. This is exemplified in Figure S8 (Supporting Information), which displays the GI-XRD pattern for a thin film on fused silica and n^+-Si with a Zr cation fraction of 0.5. Prior to deposition, all substrates were cleaned using an ultrasonic bath for 5 min in DI water, acetone, and isopropanol consecutively. All films were sputtered using a Kurt J. Lesker Company (KJLC) PVD 75 system with a base pressure of $5 \cdot 10^{-8}$ Torr and a 17 cm distance between the 2″-targets and the substrate. The Zr-Ta-N-O layers were deposited at substrate temperature set points between 500 and 600 °C with a constant rotation of 10 rpm to ensure film uniformity. Before each deposition, the Ta (99.95% purity, KJLC) and Zr (99.85% purity, KJLC) targets were first conditioned by Ar plasma sputtering (99.9999% Ar, Linde GmbH) at a pressure of 8.5 mTorr and a DC sputtering power of 60 W for 10 min. During the second half of that time, an additional radio frequency substrate bias of 20 W was applied to clean the sample surfaces via mild Ar ion bombardment immediately prior to deposition. In the next step, the process gas, consisting of 10 sccm Ar, 20 sccm N_2 (99.9999% N_2, Linde Electronics GmbH), and 0.24 sccm O_2 (99.9999% O_2, Linde Electronics GmbH), was introduced into the chamber, resulting in a deposition pressure of 6.5 mTorr. For film deposition, the power applied to the Zr and Ta targets was adjusted according to the values presented in Table S1 (Supporting Information). Film deposition was initiated by opening the substrate shutter after the applied voltages and currents to both targets had stabilized. To achieve similar film thicknesses for all Zr fractions and account for the variation of sputter rates with applied target power, the deposition time was varied from 60 to 90 min.

X-ray photoelectron spectroscopy was performed at a pass energy of 20 eV and a take-off angle of 0° using a SPECS System equipped with a non-monochromatized Al Kα (hν = 1486.6 eV) source and a PHOIBOS 100 concentric hemispherical energy analyzer with an MCD-5 detector. Data analysis was performed with the CasaXPS software using a Shirley background and GL(30) peak shapes. Due to minor charging of Zr-rich films, the peak positions presented in the main manuscript were calibrated using the carbon calibration method, applying a rigid energetic shift to all core levels to achieve an adventitious C 1s signal at 284.8 eV. Uncalibrated data can be found in Figure S5 (Supporting Information).

Elastic recoil detection analysis (ERDA) was measured at the Ion Beam Centre of the Helmholtz–Zentrum Dresden-Rossendorf. A 43 MeV Cl^{7+} ion beam was used and the angle between the sample normal and the incoming beam was fixed at 75°, with a scattering angle of 30°. The analyzed area was approx. 2×2 mm². The recoil atoms and scattered ions were detected with a Bragg ionization chamber, which enabled energy measurement and Z identification of the particles. This detector was preceded by a 25 µm Kapton foil to stop scattered ions and heavy recoil ions. The depth resolution of this system was reduced because of energy loss straggling in the foil. Data analysis was conducted using the Windf v9.3 g software.[60] The depth profiles can be calculated by using

$$t = \frac{N_M \cdot <M_Z>}{\rho \cdot N_A} \quad with \quad <M_Z> = \sum f_Z \cdot M_Z \qquad (1)$$

with t the thickness, N_M the areal density, $<M_Z>$; the average atomic mass with f_Z and M_Z the atomic fraction and the atomic weight of element Z, respectively, ρ the density, and N_A Avogadro's number.

Energy-dispersive X-ray spectroscopy (EDX) was measured using a ZEISS EVO SEM equipped with a Quantax (Bruker) X-ray detector. Measurements were performed using an incident electron energy of 20 keV and a working distance of 10 mm. Three different spots were measured and averaged for each sample to improve statistics and account for inhomogeneities.

The structure of each thin film was investigated with X-ray diffraction using a Rigaku SmartLab diffractometer equipped with a copper anode and a HyPix-3000 2D detector. Grazing incidence X-ray diffraction was measured at a fixed incidence angle ω of 0.4°, while scanning 2θ from 15° to 70° at a scan rate of 2°min^{-1} with a step size of 0.04°.

Atomic force microscopy images were obtained using a Bruker Multi-Mode operated in tapping mode with NSG30 cantilevers. Post-processing and analysis were performed using Gwydion. Grain sizes were analyzed using the watershed method.

The optical absorption characteristics were measured via the transflectance signal obtained with the diffuse reflectance accessories of an Agilent Cary 5000 spectrophotometer using a photomultiplier tube detector. The probe light from a tungsten lamp was scanned from 800 to 300 nm with a scan speed of 60 nm min^{-1}.

Variable angle spectroscopic ellipsometry (VASE) was used to model the optical constants. Spectroscopic ellipsometry was performed using an M2000 XI-210 ellipsometer by J. A. Woollam and the CompleteEASE software. Light in the range of 210-1690 nm emitted by a xenon lamp (L2174-01, 75 W, Hamamatsu) was used to analyze the optical response at angles from 45° to 75°, as well as in normal transmission. The fit model consisted of a semitransparent top layer and a fused silica substrate. All samples were fitted using a generalized oscillator model based on an initial Kramers-Kronig consistent b-spline fit. To accommodate depth-dependent variations in the thin film properties, a graded layer model, consisting of five layers, was introduced to model variations and resulted in a significant increase in the fit quality.

Contact potential difference (CPD) and surface photovoltage (SPV) measurements were performed under ambient conditions using a commercial KP020 Kelvin probe system from KP Technology. The work function of the tip was calibrated using a clean HOPG surface in air. For illumination, a 455 nm Thorlabs LED with the current adjusted to achieve SPV signal saturation, which was observed at approximately 3 mW cm^{-2}.

Supporting Information

Supporting Information is available from the Wiley Online Library or from the author.

Acknowledgements

(SolTech), and from the German Federal Ministry of Education and Research (BMBF, Germany), project SINATRA:CO2UPLED/033RC034. V.S. acknowledges support from the Bavarian Academy of Sciences and Humanities. Parts of this research were carried out by F.M. at the Ion Beam Center at the Helmholtz–Zentrum Dresden–Rossendorf e.V., a member of the Helmholtz Association.

Conflict of Interest

The authors declare no conflict of interest.

Data Availability Statement

The data that support the findings of this study are available from the corresponding author upon reasonable request.

Keywords

[1] D. Moskovskikh, S. Vorotilo, V. Buinevich, A. Sedegov, K. Kuskov, A. Khort, C. Shuck, M. Zhukovskyi, A. Mukasyan, *Sci. Rep.* **2020**, *10*, 19874.
[2] F. A. Ponce, D. P. Bour, *Nature* **1997**, *386*, 351.
[3] J. S. J. Hargreaves, *Appl. Petrochem. Res.* **2014**, *4*, 3.
[4] J. Coey, P. Smith, *J. Magn. Magn. Mater.* **1999**, *200*, 405.
[5] S. Wang, D. Antonio, X. Yu, J. Zhang, A. L. Cornelius, D. He, Y. Zhao, *Sci. Rep.* **2015**, *5*, 13733.
[6] J. B. Khurgin, *ACS Photonics* **2022**, *9*, 743.
[7] A. Kharitonov, S. Kharintsev, *Opt. Mater. Express* **2020**, *10*, 513.
[8] G. V. Naik, J. Kim, A. Boltasseva, *Opt. Mater. Express* **2011**, *1*, 1090.
[9] H. Shim, Z. Kuang, O. D. Miller, *Opt. Mater. Express* **2020**, *10*, 1561.
[10] A. L. Greenaway, C. L. Melamed, M. B. Tellekamp, R. Woods-Robinson, E. S. Toberer, J. R. Neilson, A. C. Tamboli, *Annu. Rev. Mater. Res.* **2021**, *51*, 591.
[11] W. Sun, C. J. Bartel, E. Arca, S. R. Bauers, B. Matthews, B. Orva nanos, B.-R. Chen, M. F. Toney, L. T. Schelhas, W. Tumas, J. Tate, A. Zakutayev, S. Lany, A. M. Holder, G. Ceder, *Nat. Mater.* **2019**, *18*, 732.
[12] C.-M. Jiang, L. I. Wagner, M. K. Horton, J. Eichhorn, T. Rieth, V. F. Kunzelmann, M. Kraut, Y. Li, K. A. Persson, I. D. Sharp, *Mater. Horiz.* **2021**, *8*, 1744.
[13] S. R. Bauers, A. Holder, W. Sun, C. L. Melamed, R. Woods-Robinson, J. Mangum, J. Perkins, W. Tumas, B. Gorman, A. Tamboli, G. Ceder, S. Lany, A. Zakutayev, *Proc. Natl. Acad. Sci. USA* **2019**, *116*, 14829.
[14] S. R. Bauers, D. M. Hamann, A. Patterson, J. D. Perkins, K. R. Talley, A. Zakutayev, *Jpn. J. Appl. Phys.* **2019**, *58*, SC1015.
[15] F. S. Hegner, A. Cohen, S. S. Rudel, S. M. Kronawitter, M. Grumet, X. Zhu, R. Korobko, L. Houben, C.-M. Jiang, W. Schnick, G. Kieslich, O. Yaffe, I. D. Sharp, D. A. Egger, *Adv. Energy Mater.* **2024**.
[16] Y. Xie, Y. Wang, Z. Chen, X. Xu, *ChemSusChem* **2016**, *9*, 1403.
[17] J. Eichhorn, S. P. Lechner, C.-M. Jiang, G. Folchi Heunecke, F. Munnik, I. D. Sharp, *J. Mater. Chem. A* **2021**, *9*, 20653.
[18] X. Cao, A. Sato, Y. Ninomiya, N. Yamada, *J. Phys. Chem. C* **2015**, *119*, 5327.
[19] X. Wang, H. Huang, T. Fang, J. Feng, Z. Li, Z. Zou, *J. Phys. Chem. C* **2019**, *123*, 28763.
[20] M. Harb, P. Sautet, E. Nurlaela, P. Raybaud, L. Cavallo, K. Domen, J.-M. Basset, K. Takanabe, *Phys. Chem. Chem. Phys.: PCCP* **2014**, *16*, 20548.
[21] G. Fan, X. Wang, H. Fu, J. Feng, Z. Li, Z. Zou, *Phys. Rev. Mater.* **2017**, *1*, 3.
[22] M. Kraut, E. Sirotti, F. Pantle, C.-M. Jiang, G. Grötzner, M. Koch, L. I. Wagner, I. D. Sharp, M. Stutzmann, *J. Phys. Chem. C* **2020**, *124*, 7668.
[23] L. I. Wagner, E. Sirotti, O. Brune, G. Grötzner, J. Eichhorn, S. Santra, F. Munnik, L. Olivi, S. Pollastri, V. Streibel, I. D. Sharp, *Adv. Funct. Mater.* **2024**, *34*, 4.
[24] G. Abadias, M. B. Kanoun, S. Goumri-Said, L. Koutsokeras, S. N. Dub, P. Djemia, *Phys. Rev. B* **2014**, *90*, 14.
[25] N. Sarmadian, R. Saniz, B. Partoens, D. Lamoen, K. Volety, G. Huyberechts, J. Paul, *Phys. Chem. Chem. Phys.: PCCP* **2014**, *16*, 17724.
[26] X.-Z. Wang, H. Luo, T. Muneshwar, H.-Q. Fan, K. Cadien, J.-L. Luo, *ACS Appl. Mater. Interfaces* **2018**, *10*, 40111.
[27] V. Streibel, J. L. Schönecker, L. I. Wagner, E. Sirotti, F. Munnik, M. Kuhl, C.-M. Jiang, J. Eichhorn, S. Santra, I. D. Sharp, *ACS Appl. Energy Mater.* **2024**, *7*, 4004.
[28] T. Mishima, M. Matsuda, M. Miyake, *Appl. Catalys. A: Gen.* **2007**, *324*, 77.
[29] S. M. Aouadi, M. Debessai, *J. Vac. Sci. Technol., A* **2004**, *22*, 1975.
[30] T. Lüdtke, S. Orthmann, M. Lerch, *Z. Naturforsch., B* **2017**, *72*, 305.
[31] E. Sirotti, L. I. Wagner, C.-M. Jiang, J. Eichhorn, F. Munnik, V. Streibel, M. J. Schilcher, B. März, F. S. Hegner, M. Kuhl, T. Höldrich, K. Müller-Caspary, D. A. Egger, I. D. Sharp, *Adv. Energy Mater.* **2024**.
[32] Z. Wang, D. M. Többens, A. Franz, S. Savvin, J. Breternitz, S. Schorr, *J. Mater. Chem. C* **2024**, *12*, 1124.
[33] S. J. Clarke, C. W. Michie, M. J. Rosseinsky, *J. Solid State Chem.* **1999**, 399.
[34] A. Y. Ganin, L. Kienle, G. V. Vajenine, *Eur. J. Inorg. Chem.* **2004**, *2004*, 3233.
[35] P. Scherrer, *Göttinger Nachrichten Math. Phys.* **1918**, 98.
[36] A. R. Denton, N. W. Ashcroft, *Phys. Rev. A: At., Mol., Opt. Phys.* **1991**, *43*, 3161.
[37] Y. Wang, D. Zhu, X. Xu, *ACS Appl. Mater. Interfaces* **2016**, *8*, 35407.
[38] A. L. Greenaway, S. Ke, T. Culman, K. R. Talley, J. S. Mangum, K. N. Heinselman, R. S. Kingsbury, R. W. Smaha, M. K. Gish, E. M. Miller, K. A. Persson, J. M. Gregoire, S. R. Bauers, J. B. Neaton, A. C. Tamboli, A. Zakutayev, *J. Am. Chem. Soc.* **2022**, *144*, 13673.
[39] Y. He, J. E. Thorne, C. H. Wu, P. Ma, C. Du, Q. Dong, J. Guo, D. Wang, *Chem* **2016**, *1*, 640.
[40] A. Zakutayev, *J. Mater. Chem. A* **2016**, *4*, 6742.
[41] S. H. Elder, F. J. DiSalvo, L. Topor, A. Navrotsky, *Chem. Mater.* **1993**, *5*, 1545.
[42] M. Rudolph, D. Stanescu, J. Alvarez, E. Foy, J.-P. Kleider, H. Magnan, T. Minea, N. Herlin-Boime, B. Bouchet-Fabre, M.-C. Hugon, *Surf. Coat. Technol.* **2017**, *324*, 620.
[43] B. Shirley, E. Jarochowska, *Facies* **2022**, *68*, 2.
[44] J. Klein, L. Kampermann, B. Mockenhaupt, M. Behrens, J. Strunk, G. Bacher, *Adv. Funct. Mater.* **2023**, *33*, 47.
[45] J. Mullerova, P. Sutta, *Commun. - Scient. Lett. Univ. Zilina* **2017**, *19*, 9.
[46] J. A. Woollam Company, CompleteEASE Software Manual.
[47] G. E. Jellison, F. A. Modine, *Appl. Phys. Lett.* **1996**, *69*, 371.
[48] R. D. Shannon, R. C. Shannon, O. Medenbach, R. X. Fischer, *J. Phys. Chem. Ref. Data* **2002**, *31*, 931.
[49] T. Higashi, H. Nishiyama, Y. Pihosh, Y. Wakishima, Y. Kawase, Y. Sasaki, A. Nagaoka, K. Yoshino, K. Takanabe, K. Domen, *Phys. Chem. Chem. Phys.: PCCP* **2023**, *25*, 20737.
[50] R. Inoue, M. Kitagawa, T. Nishigaki, D. Morita, K. Ichino, H. Kusano, H. Kobayashi, *Appl. Surf. Sci.* **1999**, *142*, 341.
[51] P. Hones, R. Sanjinés, F. Lévy, *Thin Solid Films* **1998**, *332*, 240.
[52] H. Cruguel, M. Guittet, O. Kerjan, F. Bart, M. Gautier-Soyer, *J. Electron Spectrosc. Relat. Phenom.* **2003**, *128*, 271.

[53] L. Casillas-Trujillo, B. Osinger, R. Lindblad, D. Karlsson, A. I. Abrikosov, S. Fritze, K. von Fieandt, B. Alling, I. Hotz, U. Jansson, I. A. Abrikosov, E. Lewin, *Mater. Chem. Front.* **2021**, *5*, 5746.

[54] S. Ke, J. S. Mangum, A. Zakutayev, A. L. Greenaway, J. B. Neaton, *Chem. Mater.* **2024**.

[55] W. N. Hansen, G. J. Hansen, *Surf. Sci.* **2001**, *481*, 172.

[56] S. Trasatti, *Pure Appl. Chem.* **1986**, *58*, 955.

[57] M. Xiao, S. Wang, S. Thaweesak, B. Luo, L. Wang, *Engineering* **2017**, *3*, 365.

[58] D. K. Singh, M. Pradhan, A. Materny, *Modern Techniques of Spectroscopy*, vol. *13*, Springer Singapore, Singapore, **2021**.

[59] D. K. Schroder, *Meas. Sci. Technol.* **2001**, *12*, R16.

[60] N. P. Barradas, C. Jeynes, R. P. Webb, *Appl. Phys. Lett.* **1997**, *71*, 291.

2400745 (10 of 10)